ASCE

Multicriteria Decision-Making Approach to Enhance Automated Anchor Pixel Selection Algorithm for Arid and Semi-Arid Regions

Yavar Pourmohamad[1]; Ahmad Ghandehari[2]; Kamran Davary[3]; and Pooya Shirazi[4]

Abstract: Finding the precise value of pixel-scale evapotranspiration (ET) for an entire basin is a major challenge to hydrologists. Many efforts have been made to conquer this challenge, among which remote sensing methods are the most promising ones. The surface energy balance algorithm for land (SEBAL) is one of the several established remote sensing methods to estimate ET. The anchor pixel selection process (e.g., hot and cold pixels) is one of the critical steps in the SEBAL model that also determines the accuracy of the model outputs. Several researchers have improved anchor pixel selection by an automated fashion. In the current study, a new simple method has been proposed to seek the best anchor pixels. Then, the daily ET outputs were assessed using observed data from the Eddy covariance (EC) tower data at Santa Cruz River Watershed for 2014–2015. The results showed that the daily ET with measured data at the study site confirmed our automated anchor pixel selection method to be reliable in terms of selecting appropriate hot and cold pixels under dry conditions by producing ET maps with reasonable accuracies ($R^2 = 0.78$ and RMSE $= 0.46$ mm day^{-1}). Our study suggests that considerations of simple image-derived parameters, such as temperature difference between hot and cold pixels, distance from a representative station, and elevation differences could improve the automatic selection of anchor pixels and the implementation of the SEBAL model under dry conditions. The machine learning technique could be combined with the proposed automated algorithm to map ET in different climates (not only arid and semiarid) faster and with more accuracy. **DOI: 10.1061/(ASCE)HE.1943-5584.0002006.**

Author keywords: Actual evapotranspiration; Endmember pixels; Search algorithm; Surface energy balance algorithm for land (SEBAL).

Introduction

A number of reports with guidelines have been issued for optimum water management by the Food and Agriculture Organization of the United Nations (FAO) (Allen et al. 1998; de Bruin et al. 2016; Doorenbos and Pruitt 1977). For optimal water management, understanding the water balance plays a crucial role (Eslami et al. 2020; Fetter 2001; Mianabadi et al. 2019; Pourmohamad et al. 2011, 2017). One of the major components of the global water cycle is ET that provides a critical nexus between terrestrial water, carbon, and surface energy exchanges (Zhang et al. 2016). It is inherently difficult to estimate the actual ET at large spatial scales because many factors control the process of ET, such as climate, water availability, terrestrial, and extraterrestrial energy are the parameters that play a role in ET determination (Gebremichael et al. 2010; Irmak et al. 2008; Zhao et al. 2013).

In several countries, the recommended method by FAO has been utilized. However, the spatial and temporal variations of the surface characteristics cannot be taken into account with high accuracy by this method (Vidal et al. 1987). Remote sensing has provided us a significant tool to assess crop water stress, either to schedule the irrigation or in the global assessment of crop water use and its spatial variations within an irrigated area by integrating more complex satellite data and computer tools (Courault et al. 2005; Pourmohamad et al. 2019).

Remote sensing might be the only feasible means to project the spatial distribution of ET over a vast landscape area. Of several remote sensing-based ET methods, two are the most common: (1) empirical/statistical relationships that link observed ET with vegetation indices [e.g., enhanced vegetation index, normalized difference vegetation index, soil-adjusted vegetation index, and leaf area index (Ramón-Reinozo et al. 2019; Singh Rawat et al. 2019)]; (2) physical models that are based on solving the surface energy balance (SEB) equation through remotely sensed estimates of land surface temperature (LST) and other terms in the SEB (Glenn et al. 2007; Kustas et al. 2003; Overgaard et al. 2005; Schmugge et al. 2002).

In the last two decades, a number of single-source surface energy balance (SSEB) models have been proposed for mapping ET, including: (1) surface energy balance algorithm for land, (2) mapping ET at high resolution with internalized calibration (METRIC), (3) simplified surface energy balance index (S-SEBI), (4) surface energy balance system (SEBS), and (5) operational simplified surface energy balance (SSEBop). Yet, there is no clear guidance on superior models under diverse conditions (Bhattarai et al. 2016). But the most common SEB model is SEBAL, which is based on the calibration of sensible heat fluxes using anchor pixels (Bastiaanssen et al. 1998a; Cunha et al. 2020; He et al. 2017; Jaafar and Ahmad 2019). Selecting the optimum anchor pixels is a challenge due to

[1]Postdoctoral Researcher, Water and Environment Research Institute, Ferdowsi Univ. of Mashhad, Azadi Square-Mashhad-Razavi Khorasan 9177948974, Iran (corresponding author). ORCID: https://orcid.org/0000-0001-9925-8658. Email: ya.pourmohamad@mail.um.ac.ir; yavar.pm@gmail.com

[2]Ph.D. Graduate, Dept. of Water Engineering and Sciences, Ferdowsi Univ. of Mashhad, Azadi Square-Mashhad-Razavi Khorasan 9177948974, Iran.

[3]Professor, Water and Environment Research Institute, Ferdowsi Univ. of Mashhad, Azadi Square-Mashhad-Razavi Khorasan 9177948974, Iran. ORCID: https://orcid.org/0000-0001-9742-4712

[4]Ph.D. Graduate, Dept. of Water Engineering and Sciences, Ferdowsi Univ. of Mashhad, Azadi Square-Mashhad-Razavi Khorasan 9177948974, Iran.

Note. This manuscript was submitted on September 21, 2019; approved on June 16, 2020; published online on September 11, 2020. Discussion period open until February 11, 2021; separate discussions must be submitted for individual papers. This paper is part of the ***Journal of Hydrologic Engineering***, © ASCE, ISSN 1084-0699.

Table 1. Anchor pixel selection revolution

No.	Authors	Satellite	Contribution
1	Allen et al. (2002b)	Landsat	• Manual selection of anchor pixels. • Introduce anchor pixel selection criteria.
2	Hodgson et al. (2004), Im et al. (2007, 2008), Im and Hodgson (2009)	QuickBird and IKONOS	• An automated calibration model for binary change detection. • Simple optimization technique in which all possible candidates are systematically considered and checked to determine if the defined statement or solution is satisfied.
3	Kjaersgaard et al. (2009)	Landsat	• Present automated selection of anchor pixels by using NDVI and surface temperature.
4	Allen et al. (2013)	Landsat	• Try to calibrate anchor pixels vegetation indices such as NDVI and surface TsDEM.
5	Bhattarai et al. (2017), Bhattarai and Liu (2019)	Landsat	• Present full-automated anchor pixel selection by using NDVI, Albedo and surface temperature. • Identification of candidate anchor pixels from homogenous agricultural fields. • Developing a GUI to calculate ET.
6	Bhattarai et al. (2019)	MODIS	• Developed an ensemble mean surface energy balance (EnSEB) modeling framework that is independent of any ground calibration.
7	Silva et al. (2019)	MODIS	• Automate the endmember pixel selection.

several parameters of concern in a large area (Paul et al. 2013). Different efforts have been made to improve anchor pixel selection. Some of them are listed in Table 1.

Your justification for the modification (existing automated approach) required is poorly described. Though several efforts have been made to automate the anchor pixel selection process in the SEBAL model, none has considered potential parameters that could further enhance the selection process. These parameters include the perimeter of a triangle that is made by anchor pixels and the station, cold and hot pixel elevation, and anchor pixel LST differences. Consideration of these parameters is essential because they add additional criteria in the process of selection of anchor pixels, especially in cases in mountainous arid and semiarid regions with sparse vegetation and spotted irrigated farms. Therefore, the proposed search algorithm (SA) was developed and evaluated in the Santa Cruz River Watershed (SCRW), Arizona.

Methods and Materials

Study Area and Data

The SCRW, located in south-central Arizona (Fig. 1), is a transboundary watershed at an elevation ranging from 608 m to 2,866 m. The SCR is an ephemeral river that drains into the Gila River, a tributary to the Colorado River (Shamir et al. 2007).

All the Arizona synoptic station hourly data were collected from the National Climatic Data Center (NNDC) for the year 2013–2014. Reference evapotranspiration (ET0) was calculated by using FAO-Penman-Monteith equations both daily and hourly scale (Allen et al. 1998). A total of 14 could free Landsat 8 OLI data on path 35 and row 38 were downloaded corresponding to the year 2013–2014 from The United States Geological Survey (USGS) website (USGS 2012).

Automation of Anchor Pixel Selection

Therefore, the SEBAL model steps and the automated anchor pixel selection algorithm for arid and semiarid regions were coded. All the codes will provide for readers on-demand. The mentioned procedure is divided into four steps: (1) the SA, (2) candidate pixel selection, (3) anchor pixels selection, and (4) SEBAL model.

SEBAL Model

To estimate instantaneous surface energy balance components, SEBAL utilizes multispectral remote sensing data accompanied with complementary meteorological data (Bastiaanssen et al. 1998a). The model is mostly applicable under clear-sky conditions when cloud-free thermal satellite data are available. Instantaneous λET (W m^{-2}) (an instantaneous latent heat flux for the time of the satellite overpass) is estimated as the remaining factor in the energy-balance equation [Eq. (1)], as the subtraction of net radiation (Rn: W m^{-2}), soil heat flux (G: W m^{-2}), and sensible heat flux (H: W m^{-2}). A full report algorithm is specified by Allen et al. (2002a, b), Bastiaanssen et al. (1998a, b)

$$\lambda ET = R_n - H - G \tag{1}$$

The following steps in a flowchart (Fig. 2) were modeled in R programing language to calculate the net radiation.

Landsat image that has been converted from digital numbers to top of atmosphere (TOA) reflectance was the input for the albedo calculation. A series of algorithms were applied that developed from various satellite sensors to determine albedo by Liang (2000). Albedo was calculated using the normalized equation by Smith as Eq. (2) (Liang 2000; Mollaei et al. 2017; Pourmohamad et al. 2019; Smith 2010)

$$\alpha = \frac{0.356\rho_2 + 0.130\rho_4 + 0.373\rho_5 + 0.085\rho_6 + 0.072\rho_7 - 0.0018}{0.356 + 0.130 + 0.373 + 0.085 + 0.072} \tag{2}$$

where ρ represents Landsat 8 reflectance for bands 2, 4, 5, 6, and 7. In the Landsat 8 data set, bands 10 and 11 were used to calculate the LST in Kelvin. To find the LST, top-atmospheric-temperatures (T_{toa}) were calculated at first using Eq. (3) for both bands 10 and 11 also in Kelvin. Then, T_{toa} were converted to LST using Eq. (4) for each band, respectively, and an average of these two bands would be an accurate estimation of the LST (Jiménez-Muñoz and Sobrino 2008; Pourmohamad et al. 2019; Yu et al. 2014)

$$T_{toa} = \frac{K2}{\ln(\frac{K1}{L_\lambda} + 1)} \tag{3}$$

$$LST = \frac{T_{toa}}{1 + (W \times (\frac{T_{toa}}{p}) \times \ln(\varepsilon_{NB})} \tag{4}$$

where K1 and K2 = thermal conversions constants for each band of 10 and 11, W = wavelength of emitted radiance (11.5 μm), p = constant equal to 14,380, which is calculated by using the Plank–Boltzmann constant and the speed of light.

Soil heat flux (G) (W m^{-2}) is the rate of the heat storage into the soil and vegetation due to conduction. SEBAL computes the ratio of G/R_n using Eq. (5) (Allen et al. 2002a). In the following equation, LST is

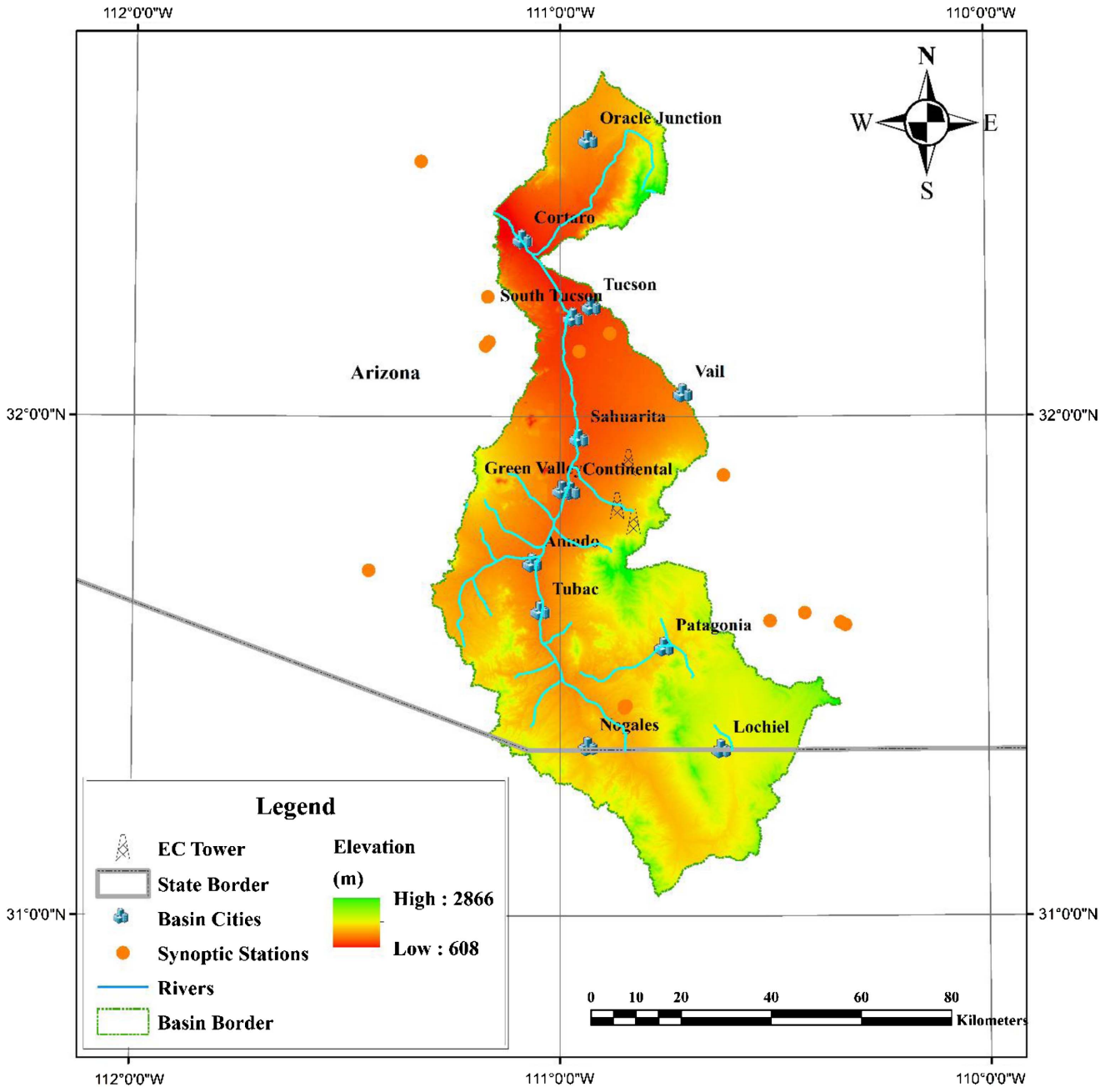

Fig. 1. Santa Cruz River Watershed. (SCRW.)

$$G/R_n = ((LST - 273.15)/\alpha)(0.0038\alpha + 0.0074\alpha^2)(1–0.98NDVI^4) \quad (5)$$

To estimate sensible heat flux (H), a set of equations was used in the form of a flowchart. Fig. 3 illustrates this loop procedure, and the loop is continued until the difference between two consecutive dT values is less than 5%.

Latent heat flux is the rate of latent heat loss from the surface due to ET. To estimate Eta, Eqs. (6)–(8) were used (Allen et al. 2002a, b)

$$ET_{inst} = 3600\frac{\lambda ET}{\lambda} \quad (6)$$

$$ETrF = \frac{ET_{inst}}{ET_r} \quad (7)$$

$$ET_a = ETrF \times ET_{r\_24} \quad (8)$$

where ET_{inst} = instantaneous ET (mm/h), ET_rF = reference ET fraction (unitless), reference ET (ET_r) computed from weather data using RefET software, ET_{r_24} = cumulative 24-h ET_r for the day of the image. Typically, ET_{r_24} is calculated only for one point, which is the synoptic station. The ET_{r_24} values from all the weather stations were interpolated into daily raster images using the inverse distance weighting (IDW) method.

Search Algorithm

In this paper, the anchor pixel selection process in the SEBAL model is treated as an optimization problem, and a new automated procedure for arid and semiarid regions is proposed by introducing a SA. Such a SA has been developed by Bhattarai et al. (2017). Their exhaustive search algorithm (ESA) has been developed and tested for a well-vegetated area such as Florida and Oklahoma

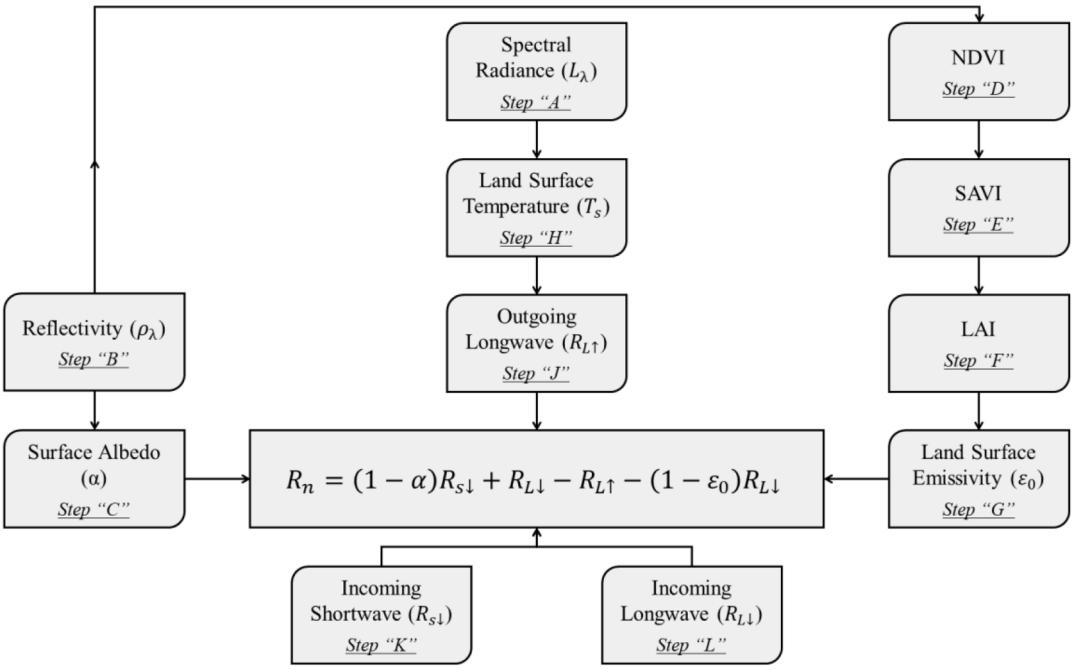

Fig. 2. Flowchart of the net surface radiation (Rn) computation. (Adapted from Allen et al. 2002a.)

(Bhattarai et al. 2017). Fig. 4 illustrates the anchor pixel selection flowchart. Comprehensive process steps are described below:

The proposed anchor pixel search algorithm consists of two main parts: (1) identification of candidate pixels from homogenous agricultural fields, and (2) application of the SA.

Candidate Pixel Selection

Sometimes the best criteria for cold pixel occurs in high altitude, which is not the SEBAL model preferences if the synoptic station is located far from the potential cold pixel or at a different elevation. The anchor pixel candidates with more than 5% slope were omitted to direct the algorithm to choose the candidate pixel.

A scoring system was applied to locate the candidate pixels. The properties by which anchor pixels were scored are based on are soil-adjusted vegetation index (SAVI), leaf area index (LAI), and albedo. The anchor pixels albedo value must be standing in a range that is suggested in different kinds of literature (Allen et al. 2002a, 2007; Long and Singh 2013; Narraway 2011; Shafian and Maas 2015). As illustrated in Fig. 4, the albedo ranges for cold and hot pixels are ranged between 0.22–0.24 and 0.13–0.15, respectively. To identify the full vegetative cultivated agricultural pixel (cold) and uncultivated agricultural pixel (hot), the top and bottom 10% of NDVI, SAVI, and LAI were chosen, respectively. These boundaries were chosen after much trial and error from 1%–10%. It was found out that 10% will guarantee finding candidate pixels to meet all other constraints.

Anchor Pixels Selection

The results of anchor pixel candidates were obtained after the identification of candidate pixels from homogenous agricultural fields (a large agricultural field that is larger than 90 m × 90 m). To select the best anchor pixel, a triangle of the synoptic station, cold and hot pixels should have the least geometry. Because the SEBAL model assumes no exchange of sensible heat in the cold pixel (i.e., H = 0), ET at this pixel is considered as ET0. Also, it is important not to select cold and hot pixels far away from each other, the reason laid in the fact that the distance between anchor pixels might lead to a heterogeneous environment for each hot and cold pixel and cause a problem in the best anchor pixel selection. In this respect, Eq. (9) describes how the distance between the cold pixel and synoptic station (d_{c-s}) was multiplied by two, the distance between hot and cold pixel (d_{c-h}) was multiplied by one and a half, and the distance between the hot pixel and the synoptic station (d_{h-s}) remains as it is

$$Triangle\ Perimeter = \log(2d_{c-s} + 1.5d_{c-h} + d_{h-s}) \quad (9)$$

However, the triangle perimeter coefficient may not be enough to distinguish the best anchor pixel. The hot and cold pixel temperature difference (dT_{h-c}) and the absolute value of anchor pixels elevation difference (dE_{h-c}) are important as well. Therefore, a decision coefficient was introduced to consider both temperature and elevation differences and described as follows [Eq. (10)]:

$$Decision\ Coefficient = dT_{h-c}^3/(Triangle\ Perimeter \times dE_{h-c}^{0.7}) \quad (10)$$

At last, all the decision coefficients are sorted, and candidate pixels with the highest score are selected as the best anchor pixels.

If the best anchor pixels trapped in the aerodynamic resistance to heat calculation loop are more than eight iterations (one should be noted that the proposed search algorithm was run many times and every time the iteration stopped between two and three iterations), the second-best anchor pixel will be selected automatically.

Model Evaluation

The SEBAL model, with the proposed approach for automated anchor pixel selection (referred to as SA-automated, hereafter), was coded in R (R Core Team 2013). The evaluation of the proposed automated approach was based on the ability to recognize anchor pixels in an image and to estimate daily ET at an ET measurement site. In the current study, frequently used model evaluation parameters [R^2, Pearson's coefficient correlation (r)] and root mean square error (RMSE) were applied.

Daily ETa estimates by the SA-automated model and manual anchor pixel selection, were evaluated and compared using measured daily ET at the EC tower stations in Arizona. EC towers were

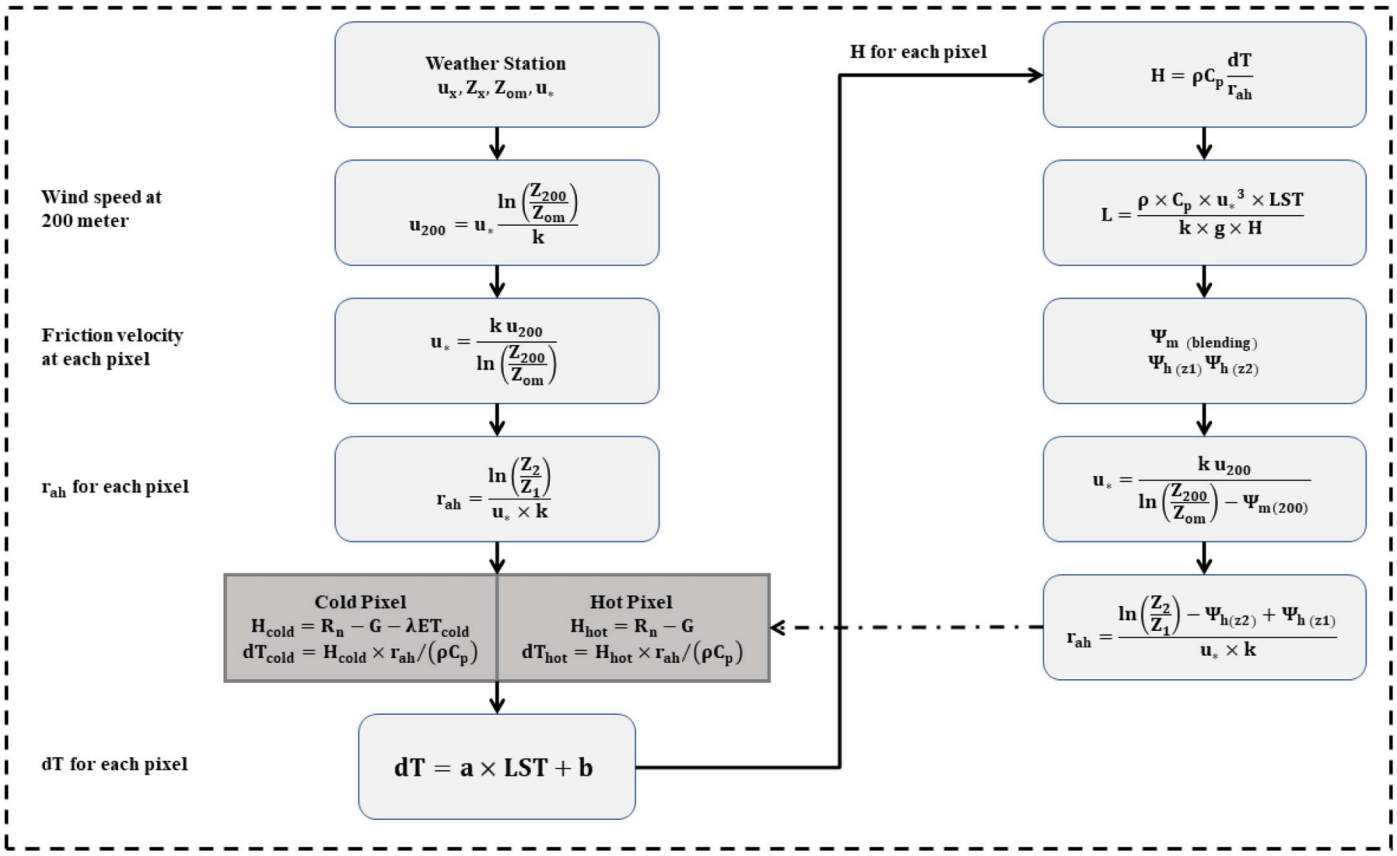

(a)

u_x is the wind speed (m/s) at height zx	u_* is the friction velocity (m/s)	Z_{om} is the momentum roughness length (m)
dT (K) is the temperature difference (T1 – T2) between two heights (z1 and z2) of anchor pixels	k is von Karman's constant (0.41)	r_{ah} is the aerodynamic resistance to heat transport (s/m)
a & b are the correlation coefficients	ρ is air density (kg/m3)	C_p is air specific heat (1004 J/kg/K)
L is Monin-Obukhov length	Ψ_h is the stability corrections for heat transport	$\Psi_{m\ (blending)}$ is the stability corrections for momentum

(b)

Fig. 3. (a) Flowchart of the iterative process for the calculation of sensible heat (H) (based on Allen et al. 2002a); and (b) notation definition for all the parameters.

commonly used to provide ETa measurements (Zitouna-Chebbi et al. 2018). FLUXNET network EC data have been obtained for 2014 at three stations of Walnut Gulch Kendall Grasslands (US-Wkg) in a small, intensively-studied, and experimental watershed (SCRW). EC tower measurements of energy, water, and CO_2 fluxes began in the spring of 2004 and ended in 2014. US-Wkg EC tower data properties are listed in Table 2 (Scott 2016).

To compare the SA-automated SEBAL and measured ET, a subset of days with available Landsat data (Table 3) was considered, when the cloud cover was less than 10%. This eliminated nine out of 23 images.

Results and Discussion

Anchor Pixel Attributes Comparison

The SA-automated model successfully captured hot and cold pixels for all images. Figs. 5(a–d) are illustrating the NDVI, SAVI, LAI, and LST density of SCRW for the year 2014, respectively. The NDVI, SAVI, and LAI density curves have almost the same bell-shape for seven images from February 22nd to June 30th. On the other hand, NDVI, SAVI, and LAI density curves on July 16th and September 2nd have entirely different shapes. The density

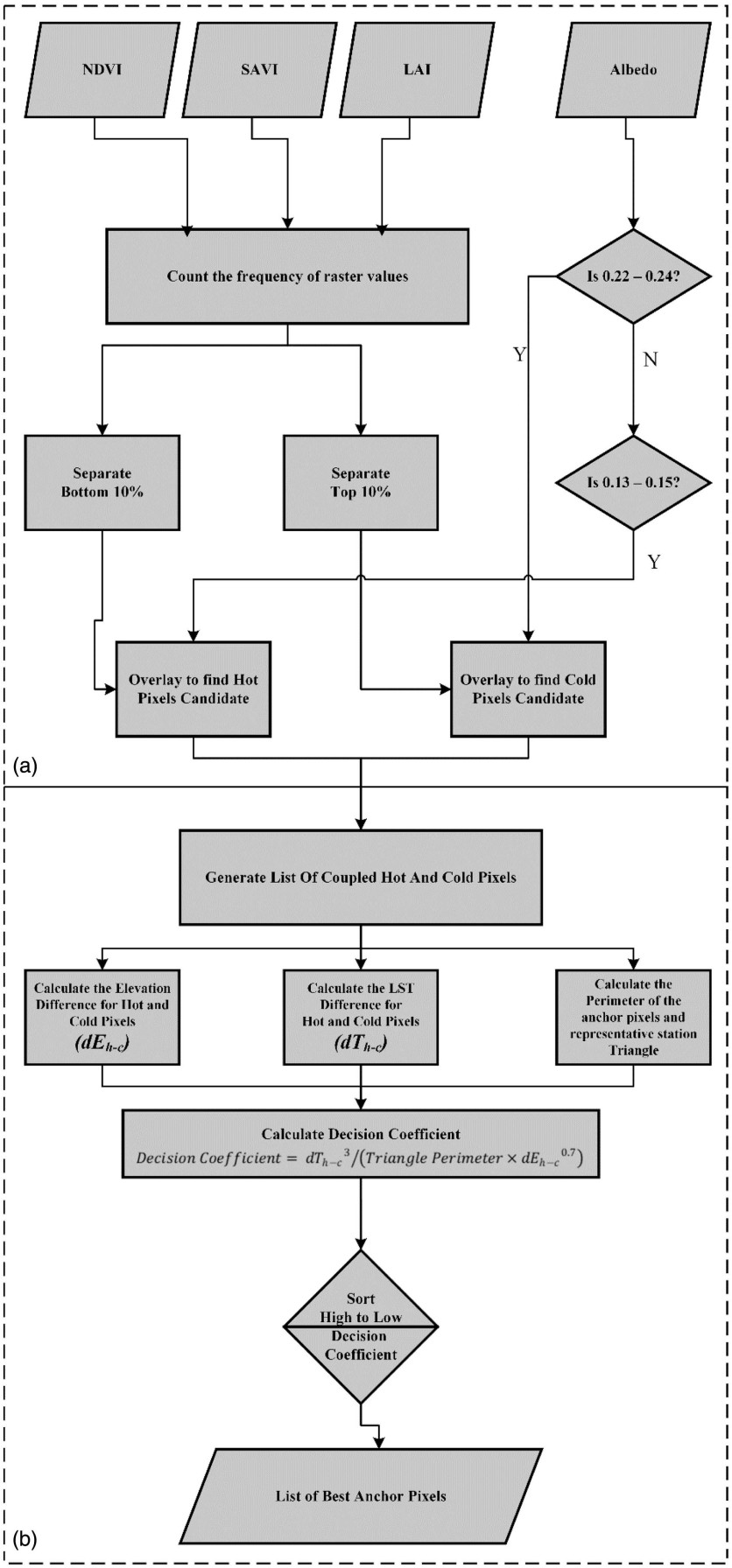

Fig. 4. Proposed method for automated selection of anchor pixels in SEBAL: (a) Identification of candidate pixels from homogenous agricultural fields; and (b) Best anchor pixels selection from the candidate list.

Table 2. US-Wkg EC tower data properties

Site ID	Descriptions
Site name	Walnut Gulch Kendall Grasslands
Tower team	PI: Russell Scott—United States Department of Agriculture Technician: Ross Bryant—USDA-ARS-SWRC
Latitude	31.7365
Longitude	−109.9419
Elevations (m)	988, 1,121, 1,289
Network	AmeriFlux
IGBP	GRA (Grasslands)
Mean annual temperature (°C)	15.64
Mean annual precipitation (mm)	407
Data products	FLUXNET2015 Dataset FLUXNET LaThuile Dataset
Data availability	FLUXNET2015: 11 years (Duration: 2004–2014) FLUXNET LaThuile: 3 years (Duration: 2004–2006)

Table 3. List of Landsat images used in this study

No.	Date	Julian day	Path/row
1	Feb 22, 2014	53	36/38
2	Mar 10, 2014	69	36/38
3	Mar 26, 2014	85	36/38
4	Apr 27, 2014	117	36/38
5	May 13, 2014	133	36/38
6	Jun 14, 2014	165	36/38
7	Jun 30, 2014	181	36/38
8	Jul 16, 2014	197	36/38
9	Sep 2, 2014	245	36/38

curves for these two dates spread almost through all the values. The vegetation density increased as the vegetation indexes have been distributed to the higher value.

Fig. 5(d) shows the LST (°K) density curves through 2014. Over time, the surface temperature has increased as the density curves have shifted to the right side. In July and September images, not only the surface temperature decreased dramatically in comparison with trends, but also it contains a broader range of surface temperature and not following the bell-shape format.

Blue and red lines in Fig. 5 are locating cold and hot pixel values, respectively. It could not be defined as an exact range of values for cold pixels on each vegetation index. The following statement is undeniable in Fig. 5. On the other hand, the hot pixel vegetation indexes values almost have the same range.

The SA flowchart [Fig. 4(a)] inputs are albedo, NDVI, SAVI, and LAI. Albedo must range between 0.22–0.24 for cold pixels and 0.13–0.15 for hot pixels (Allen et al. 2002b; Aoki et al. 1992). To find the candidate anchor pixels, top n% (n = 10) and bottom n% of NDVI, SAVI, and LAI are the targets. But in most of the previous studies, the LST is one of the variables to find the candidate pixels. In the current study, LST has not taken into account finding the candidate pixels but plays a significant role in choosing the best candidates as anchor pixels. Therefore, the anchor pixel values for NDVI, SAVI, and LAI are located at the top and bottom in Figs. 5(a–c), respectively.

Fig. 4(b) and Eqs. (9) and (10) are describing the best anchor pixel selection procedure. The main contribution of the current study was a scoring system that considers all three variables of the triangle perimeter [Eq. (9)], anchor pixel elevation difference, and temperature difference. Many different coefficients and relationships among those three variables have been tested surfaces, and the results were evaluated by EC towers data to come up with Eq. (10). The properties for the best anchor pixel are described as follows: (1) maximum temperature difference between hot and cold pixel, (2) minimum distance between anchor pixels and synoptic station, and (3) minimum hot and cold pixel elevation difference. Eq. (10) describes how these properties were considered. Fig. 5(d) shows the hot and cold pixel LST value.

Fig. 6 illustrates the elevation density curve of SCRW. In addition, blue and red lines are cold and hot pixel locations, respectively, which are located almost at the same elevation.

Finding the hot and cold pixels with most temperature differences is not enough because of two reasons: (1) elevation differences would cause significant temperature differences, (2) SEBAL tries to find sensible heat flux by finding optimum aerodynamic resistance to heat transport ($r_{ah:}$ s/m) through temperature differences at hot and cold pixels; therefore, hot and cold pixels not only must be close but also to have the best result they require to be almost at the same elevation. Fig. 6 clearly suggests that the SA results by considering the previous statement.

The exact selected anchor pixels' properties are described in Table 4. The SA-automated model selected the same elevation (~900 m) in June and a higher altitude (~1,200 m) in July. In the following, the anchor pixel elevations for the remaining images are between 718 and 794 m.

Both cold and hot pixels on July 16th have a lower surface temperature value in comparison with the one on June 30th and September 2nd. This phenomenon can be explained by comparing the surface temperature density, which is shifted to the left side (lower surface temperature) and anchor pixel elevation (~1,200 m above sea level) on July 16th with two images before and after. The cumulative precipitation (mm) and a number of rainy days that occurred in the last 16 days prior to each image are presented in Table 5. Because of the precipitation on July 2nd for 14 days and 61.9 mm depth, the LST decreased dramatically, as showed in Fig. 5. Almost the same situation happened for the image on September 2nd. But the precipitation ended four days earlier on August 30th. As a result, the LST density curve has shifted to the right side, higher LST comparing with the LST on July 16th (Trenberth and Shea 2005).

Daily ET Evaluation from the New Automated Method

Fig. 7 demonstrates the remote sensed calculated ETa using the SA-automated model (on the left) and manually selected anchor pixels (on the right) on the Y axis versus measured ETa at EC towers on the X axis. Because the ETa was measured at three elevations (988, 1,121, and 1,289 m above sea level) by three EC towers, the measured and calculated ETa were grouped by their elevations.

The variation in measured daily ETa for Landsat acquisition dates at the four sites was in a good agreement with SA-automated SEBAL model counterparts ($R^2 = 0.78$ and RMSE = 0.46 mm day^{-1}). But on the other hand, the manual approach does not correlate as good as the SA-automated model ($R^2 = 0.76$ and RMSE = 0.50 mm day^{-1}).

The blue dots represent ETa at 1,289 m above sea level, which is mostly placed out of the confidence interval. On the other hand, the red dots (988 m above sea level) all located within the confidence interval. The green dots (1,121 m above sea level) fall somewhere in between. It is noted that the synoptic station elevation is at 1,050 m above sea level. ETa evaluation results showed that there is a direct relationship between weather station elevation and the

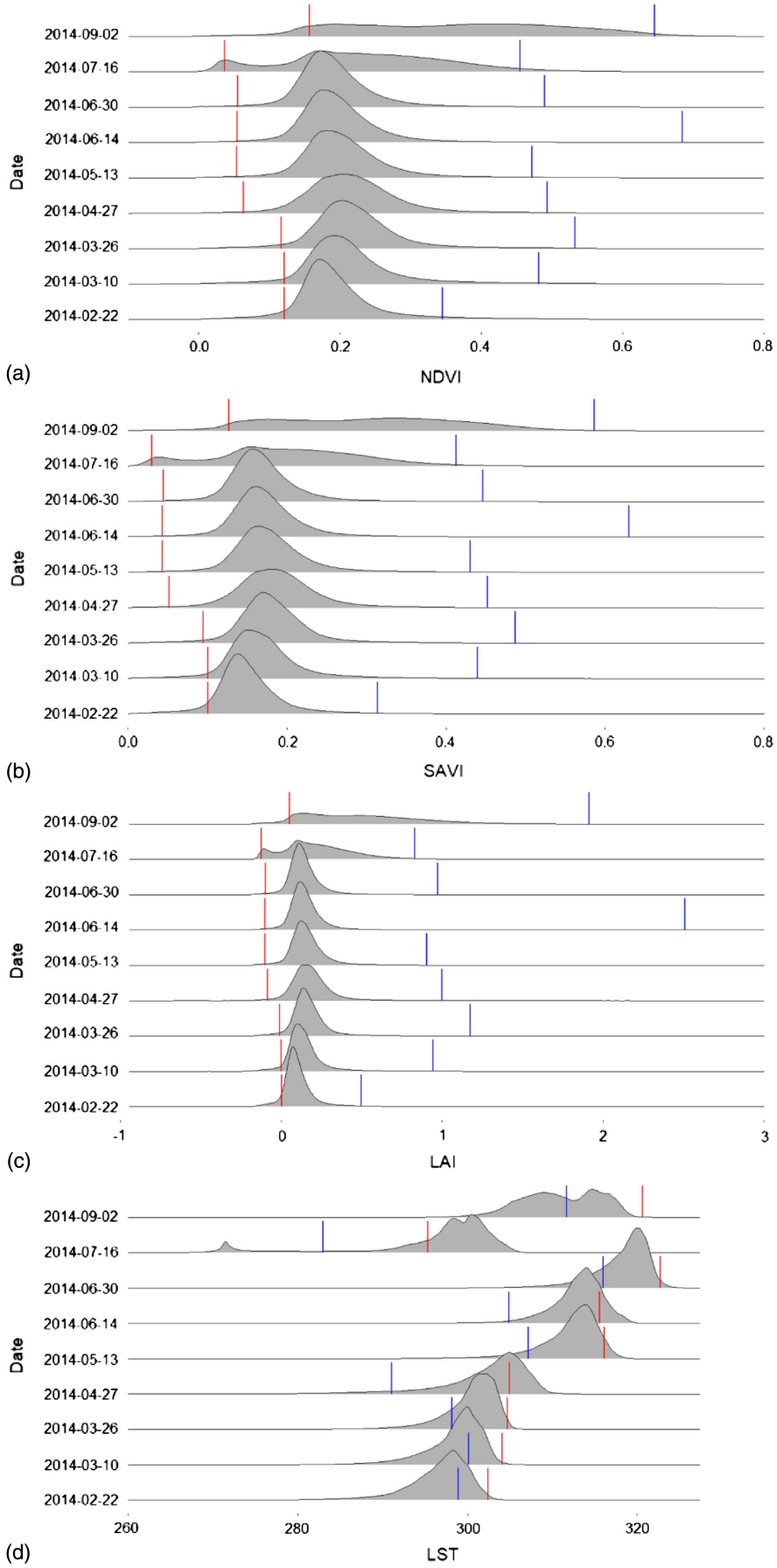

Fig. 5. Density of (a) NDVI; (b) SAVI; (c) LAI; and (d) LST for the year 2014 in SCRW and best anchor pixel selection place. (The left line refers to cold pixel, and the right line refers to hot pixel.)

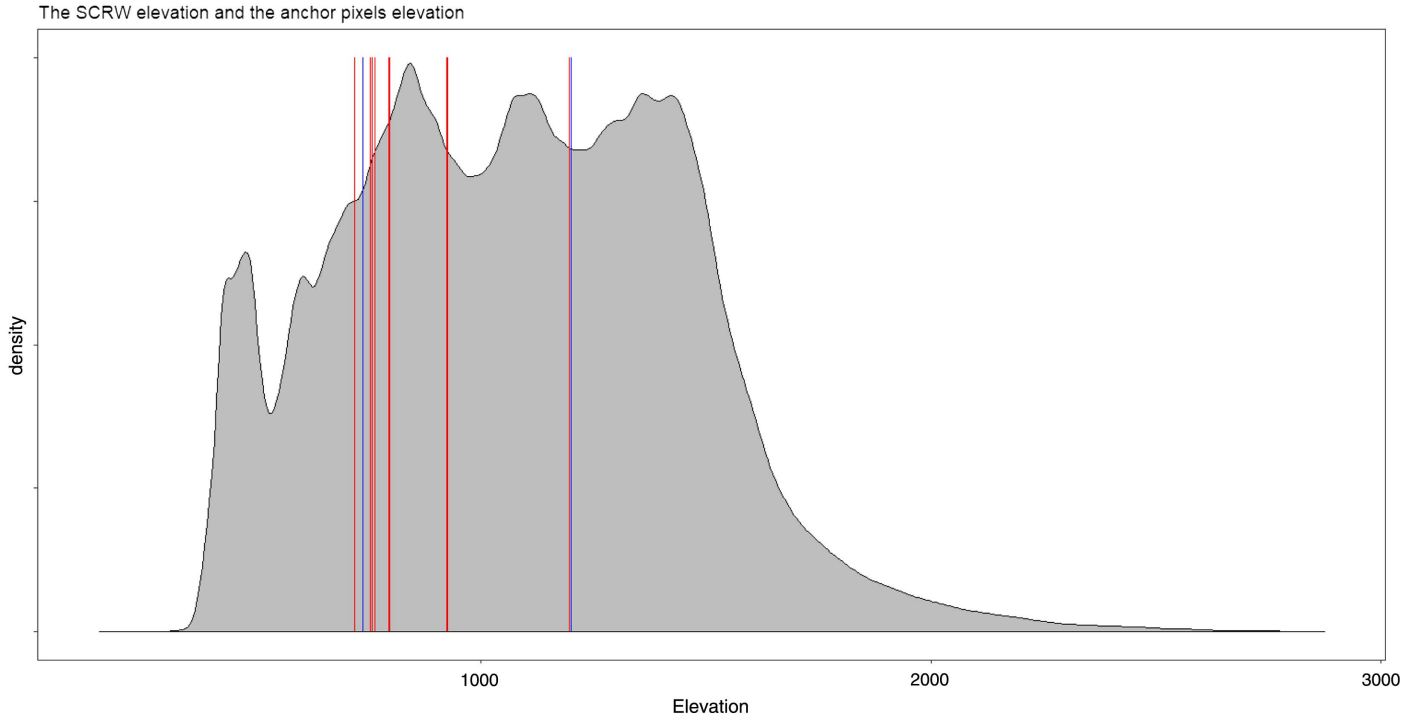

Fig. 6. Elevation density curve of the SCRW and blue and red lines are cold and hot pixel locations, respectively.

Table 4. Selected anchor pixel properties

No.	Date	Elevation cold	Elevation hot	SAVI cold	SAVI hot	NDVI cold	NDVI hot	LAI cold	LAI hot	LST cold	LST hot
1	Feb 22	737.76	718.51	0.31	0.10	0.35	0.12	0.50	0.001	298.94	302.41
2	Mar 10	753.11	753.12	0.44	0.10	0.48	0.12	0.94	0.001	300.14	304.08
3	Mar 26	764.55	764.55	0.49	0.10	0.53	0.12	1.17	−0.009	298.19	304.71
4	Apr 27	797.00	797.00	0.45	0.05	0.49	0.06	1.00	−0.086	291.04	304.98
5	May 13	794.05	794.36	0.43	0.04	0.47	0.05	0.90	−0.101	307.18	316.13
6	Jun 14	924.57	924.57	0.63	0.04	0.68	0.05	2.51	−0.101	304.88	315.59
7	Jun 30	925.52	925.52	0.45	0.04	0.49	0.06	0.97	−0.099	316.01	322.73
8	Jul 16	1,199.35	1,196.29	0.41	0.03	0.45	0.04	0.83	−0.123	282.97	295.30
9	Sep 2	758.02	757.99	0.59	0.13	0.65	0.16	1.91	0.052	311.71	320.64

Table 5. Precipitation depth that occurred within 16 days prior to each image

Date	Precipitation (mm)	Rainy days
22 Feb	2	2
10 Mar	49.7	7
26 Mar	0.4	4
27 Apr	2.9	5
13 May	0.7	3
14 Jun	0.4	2
30 Jun	0	0
16 Jul	61.9	14
2 Sep	61.3	10

accuracy of the calculated ETa. The same advice was given in some previous studies (Allen et al. 2002b, 2011).

Conclusion

A simple optimization technique in the form of an SA-automated can reduce the need for cumbersome manual component input in the SEBAL model. The proposed two-stage automated approach first uses a simple decision tree-based classifier to detect candidate anchor pixels from homogenous agricultural fields for use in the iterative search process. The SA-automated is then applied to examine the candidate pixels based on a triangle perimeter with vertices of the synoptic station, endmember anchor pixel locations, the anchor pixel difference in elevation, and surface temperature to select the hot and cold pixels. The model was verified under relatively dry weather in Arizona's Santa Cruz River Watershed. The pixel-level comparison and evaluation of daily ET with measured data at the study site indicated that using our automated anchor pixel selection method in the SEBAL model generates satisfactory results ($R^2 = 0.78$ and RMSE $= 0.46$ mm day^{-1}) with the consistent selection of suitable hot and cold pixels under dry conditions.

Selecting the hot and cold pixels based on their morphological properties is one of the hypotheses that was tested in this study. The hot and cold pixels are known as wet, well-irrigated crop surfaces having full ground cover by vegetation and a dry, bare agricultural field, respectively. Therefore, LST involvement as a parameter to select the anchor pixels is omitted. So, in this study, it was tried to select anchor pixels to differ from Bhattarai et al. (2017). Concerning the SA-automated model proposed, candidate anchor pixels are

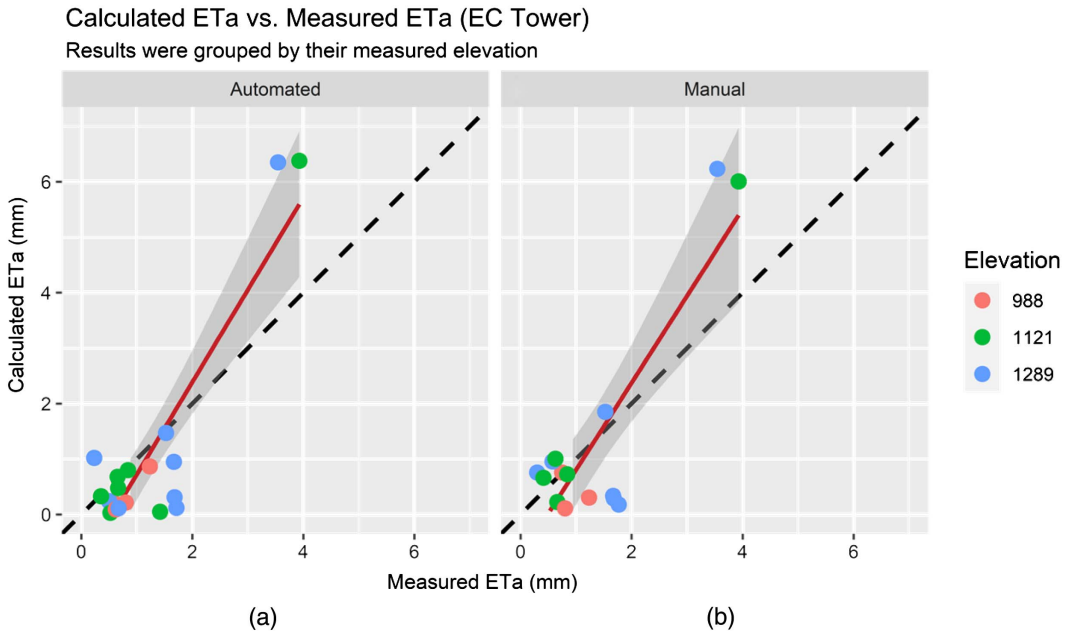

Fig. 7. (a) Remote sensed calculated ETa using SA-automated model; and (b) remote sensed calculated ETa using the manually selected hot and cold pixels, versus measured ETa at EC towers. The dashed line represents the bisector, whereas the red line is the linear fitted trendline, and the shadow part is the confidence interval with confidence interval equal to 0.95.

based only on their morphological properties and involve LST and other parameters (e.g., distances and elevations) as an auxiliary parameter to rank the coupled cold and hot pixels. Because cold and hot pixel LST are affected by the elevation (considering the LST and near-surface air temperature differences is the basis of the SEBAL), the proposed method involves the cold and hot elevation differences as a parameter to rank the anchor pixels candidates. Such modification enhances the anchor pixel selection performance by accounting for the essence of the cold and hot pixels along with ET estimation.

Although the automation process improves model performance and reliability in terms of time and function and enhances the capacity for operational applications and creates new multimodel ET models. Besides, potential bias in ET estimation for new or inexperienced users can be reduced by the application of the automation approach and consequently bring these models within the domain of such users. Future studies will test the performance and accuracy of the proposed SA-automated model in different locations with different climates and integrating the machine learning to choose the best criteria to find anchor pixels. Machine learning algorithms may capture precipitation, irrigation, or some dynamic changes in the agricultural fields and improve the anchor pixel selection process (Bannayan et al. 2011; Molina-Navarro et al. 2016).

Data Availability Statement

All data, models, or code generated or used during the study are available from the corresponding author by request.

Acknowledgments

Our special thanks go to USGS, FLUXNET community and National Climatic Data Center for providing us with the Landsat 8 dataset, eddy covariance, and synoptic station data. Also, we thank Dr. Nishan Bhattarai University of Michigan for helping us to develop the algorithm.

References

Allen, R. G., et al. 2007. "Satellite-based energy balance for mapping evapotranspiration with internalized calibration (METRIC)—Applications." *J. Irrig. Drain. Eng.* 133 (4): 395–406. https://doi.org/10.1061/(ASCE)0733-9437(2007)133:4(395).

Allen, R. G., B. Burnett, W. Kramber, J. Huntington, J. Kjaersgaard, A. Kilic, C. Kelly, and R. Trezza. 2013. "Automated calibration of the METRIC-Landsat evapotranspiration process." *J. Am. Water Resour. Assoc.* 49 (3): 563–576. https://doi.org/10.1111/jawr.12056.

Allen, R. G., L. S. Pereira, T. A. Howell, and M. E. Jensen. 2011. "Agricultural water management evapotranspiration information reporting. I: Factors governing measurement accuracy." *Agric. Water Manage.* 98 (6): 899–920. https://doi.org/10.1016/j.agwat.2010.12.015.

Allen, R. G., L. S. Pereira, D. Raes, and M. Smith. 1998. "Crop evapotranspiration-Guidelines for computing crop water requirements-FAO Irrigation and drainage paper 56." *Fao, Rome* 300 (9): D05109.

Allen, R. G., M. Tasumi, R. Trezza, R. Waters, and W. Bastiaanssen. 2002a. *Surface energy balance algorithm for land (SEBAL)—Advanced training and users manual*. Kimberly, South Africa: Idaho Implementation.

Allen, R. G., R. Trezza, and M. Tasumi. 2002b. *Surface energy balance algorithms for land. Advance training and users manual, version 1.0*. Moscow, ID: Univ. of Idaho.

Aoki, M., I. Horiguchi, C. Itoh, G. Q. Yang, T. Harada, and T. Yakuwa. 1992. "Development of an aseptic plant tissue culture vessel system enabling ventilation, air composition control, and addition of nutrient solutions." *J. Agric. Meteorol.* 48 (1): 29–37. https://doi.org/10.2480/agrmet.48.29.

Bannayan, M., S. S. Lotfabadi, S. Sanjani, A. Mohamadian, and M. Aghaalikhani. 2011. "Effects of precipitation and temperature on crop production variability in northeast Iran." *Int. J. Biometeorol.* 55 (3): 387–401. https://doi.org/10.1007/s00484-010-0348-7.

Bastiaanssen, W. G. M., M. Menenti, R. A. Feddes, and A. A. M. Holtslag. 1998a. "A remote sensing surface energy balance algorithm for land (SEBAL). 1. Formulation." *J. Hydrol.* 212 (Dec): 198–212. https://doi.org/10.1016/S0022-1694(98)00253-4.

Bastiaanssen, W. G. M., H. Pelgrum, J. Wang, Y. Ma, J. F. Moreno, G. J. Roerink, and T. Van der Wal. 1998b. "A remote sensing surface energy balance algorithm for land (SEBAL).: Part 2: Validation." *J. Hydrol.* 212 (Dec): 213–229. https://doi.org/10.1016/S0022-1694(98)00254-6.

Bhattarai, N., and T. Liu. 2019. "LandMOD ET mapper: A new Matlab-based graphical user interface (GUI) for automated implementation of SEBAL and METRIC models in thermal imagery." *Environ. Modell. Software* 118 (Aug): 76–82. https://doi.org/10.1016/j.envsoft.2019.04.007.

Bhattarai, N., K. Mallick, J. Stuart, B. D. Vishwakarma, R. Niraula, S. Sen, and M. Jain. 2019. "An automated multi-model evapotranspiration mapping framework using remotely sensed and reanalysis data." *Remote Sens. Environ.* 229 (Aug): 69–92. https://doi.org/10.1016/j.rse.2019.04.026.

Bhattarai, N., L. J. Quackenbush, J. Im, and S. B. Shaw. 2017. "A new optimized algorithm for automating endmember pixel selection in the SEBAL and METRIC models." *Remote Sens. Environ.* 196 (Jul): 178–192. https://doi.org/10.1016/j.rse.2017.05.009.

Bhattarai, N., S. B. Shaw, L. J. Quackenbush, J. Im, and R. Niraula. 2016. "Evaluating five remote sensing based single-source surface energy balance models for estimating daily evapotranspiration in a humid subtropical climate." *Int. J. Appl. Earth Obs. Geoinf.* 49 (Jul): 75–86. https://doi.org/10.1016/j.jag.2016.01.010.

Courault, D., B. Seguin, and A. Olioso. 2005. "Review on estimation of evapotranspiration from remote sensing data: From empirical to numerical modeling approaches." *Irrig. Drain. Syst.* 19 (3–4): 223–249. https://doi.org/10.1007/s10795-005-5186-0.

Cunha, J., T. E. Pereira, E. Pereira, I. Rufino, C. Galvão, F. Valente, and F. Brasileiro. 2020. "A high-throughput shared service to estimate evapotranspiration using Landsat imagery." *Comput. Geosci.* 134 (Apr): 104341. https://doi.org/10.1016/j.cageo.2019.104341.

de Bruin, H. A. R., I. F. Trigo, F. C. Bosveld, and J. F. Meirink. 2016. "A Thermodynamically based model for actual evapotranspiration of an extensive grass field close to FAO reference, suitable for remote sensing application." *J. Hydrometeorol.* 17 (5): 1373–1382. https://doi.org/10.1175/JHM-D-15-0006.1.

Doorenbos, J., and W. O. Pruitt. 1977. *Guidelines for predicting crop water requirements, FAO-ONU*. Irrigation and Drainage Paper 24, 144. Rome: Food and Agriculture Organization of the United Nations.

Eslami, Z., S. Janatrostami, A. Ashrafzadeh, and Y. Poumohamad. 2020. "Water, energy, food nexus approach impact on integrated water resources management in sefid-rud irrigation and drainage network." *J. Water Soil* 34 (1): 11–25. https://doi.org/10.22067/jsw.v34i1.81897.

Fetter, C. W. 2001. *Applied hydrogeology.* Long Grove, IL: Waveland Press.

Gebremichael, M., J. Wang, and T. W. Sammis. 2010. "Dependence of remote sensing evapotranspiration algorithm on spatial resolution." *Atmos. Res.* 96 (4): 489–495. https://doi.org/10.1016/j.atmosres.2009.12.003.

Glenn, E. P., A. R. Huete, P. L. Nagler, K. K. Hirschboeck, and P. Brown. 2007. "Integrating remote sensing and ground methods to estimate evapotranspiration." *Crit. Rev. Plant Sci.* 26 (3): 139–168. https://doi.org/10.1080/07352680701402503.

He, R., Y. Jin, M. M. Kandelous, D. Zaccaria, B. L. Sanden, R. L. Snyder, J. Jiang, and J. W. Hopmans. 2017. "Evapotranspiration estimate over an almond orchard using Landsat satellite observations." *Remote Sens.* 9 (5): 436. https://doi.org/10.3390/rs9050436.

Hodgson, M. E., X. Li, and Y. Cheng. 2004. "A parameterization model for transportation feature extraction." *Photogramm. Eng. Remote Sens.* 70 (12): 1399–1404. https://doi.org/10.14358/PERS.70.12.1399.

Im, J., and M. E. Hodgson. 2009. "Characteristics of search spaces for identifying optimum thresholds in change detection studies." *GISci. Remote Sens.* 46 (3): 249–272. https://doi.org/10.2747/1548-1603.46.3.249.

Im, J., J. R. Jensen, and M. E. Hodgson. 2008. "Optimizing the binary discriminant function in change detection applications." *Remote Sens. Environ.* 112 (6): 2761–2776. https://doi.org/10.1016/j.rse.2008.01.007.

Im, J., J. Rhee, J. R. Jensen, and M. E. Hodgson. 2007. "An automated binary change detection model using a calibration approach." *Remote Sens. Environ.* 106 (1): 89–105. https://doi.org/10.1016/j.rse.2006.07.019.

Irmak, S., E. Istanbulluoglu, and A. Irmak. 2008. "An evaluation of evapotranspiration model complexity against performance in comparison with Bowen ratio energy balance measurements." *Trans. ASABE Am. Soc. Agri. Biol. Eng.* 51 (4): 1295–1310. https://doi.org/10.13031/2013.25246.

Jaafar, H. H., and F. A. Ahmad. 2019. "Time series trends of Landsat-based ET using automated calibration in METRIC and SEBAL: The Bekaa Valley, Lebanon." *Remote Sens. Environ.* 238 (Mar): 111034. https://doi.org/10.1016/j.rse.2018.12.033.

Jiménez-Muñoz, J. C., and J. A. Sobrino. 2008. "Split-window coefficients for land surface temperature retrieval from low-resolution thermal infrared sensors." *IEEE Geosci. Remote Sens. Lett.* 5 (4): 806–809. https://doi.org/10.1109/LGRS.2008.2001636.

Kjaersgaard, J. H., R. G. Allen, M. Garcia, W. Kramber, and R. Trezza. 2009. *Automated selection of anchor pixels for Landsat based evapotranspiration estimation*. , 1–11. Reston, VA: ASCE.

Kustas, W. P., J. M. Norman, M. C. Anderson, and A. N. French. 2003. "Estimating subpixel surface temperatures and energy fluxes from the vegetation index–radiometric temperature relationship." *Remote Sens. Environ.* 85 (4): 429–440. https://doi.org/10.1016/S0034-4257(03)00036-1.

Liang, S. 2000. "Narrowband to broadband conversions of land surface albedo I: Algorithms." *Remote Sens. Environ.* 76 (2): 213–238. https://doi.org/10.1016/S0034-4257(00)00205-4.

Long, D., and V. P. Singh. 2013. "Assessing the impact of end-member selection on the accuracy of satellite-based spatial variability models for actual evapotranspiration estimation." *Water Resour. Res.* 49 (5): 2601–2618. https://doi.org/10.1002/wrcr.20208.

Mianabadi, A., M. Coenders-Gerrits, P. Shirazi, B. Ghahraman, and A. Alizadeh. 2019. "A global Budyko model to partition evaporation into interception and transpiration." *Hydrol. Earth Syst. Sci.* 23 (12): 4983–5000. https://doi.org/10.5194/hess-23-4983-2019.

Molina-Navarro, E., M. Hallack-Alegría, S. Martínez-Pérez, J. Ramírez-Hernández, A. Mungaray-Moctezuma, and A. Sastre-Merlín. 2016. "Hydrological modeling and climate change impacts in an agricultural semiarid region. Case study: Guadalupe River basin, Mexico." *Agric. Water Manage.* 175 (Sep): 29–42. https://doi.org/10.1016/j.agwat.2015.10.029.

Mollaei, Z., K. Davary, S. Majid Hasheminia, A. Faridhosseini, and Y. Pourmohamad. 2017. "Enhancing flood hazard estimation methods on alluvial fans using an integrated hydraulic and geological and geomorphological approach." *Nat. Hazards Earth Syst. Sci.* 18 (4): 1159–1171. https://doi.org/10.5194/nhess-18-1159-2018.

Narraway, R. 2011. *Encyclopedia of soil science*. 2nd ed. London: Taylor & Francis.

Overgaard, J., D. Rosbjerg, and M. B. Butts. 2005. "Land-surface modelling in hydrological perspective." *Biogeosci. Discuss.* 2 (6): 1815–1848. https://doi.org/10.5194/bgd-2-1815-2005.

Paul, G., P. H. Gowda, P. V. V. Prasad, T. A. Howell, R. M. Aiken, and S. L. Hutchinson. 2013. *Role of hot and cold pixel concept in remote sensing based single source surface energy balance algorithms.* , 103–117. Phoenix: US Committee on Irrigation and Drainage.

Pourmohamad, Y., A. Alizadeh, M. Mousavi Baygi, M. Gebremichael, A. N. Ziaei, and M. Bannayan. 2019. "Optimizing cropping area by proposing a combined water-energy productivity function for Neyshabur Basin, Iran." *Agric. Water Manage.* 217 (Jul): 131–140. https://doi.org/10.1016/j.agwat.2019.02.040.

Pourmohamad, Y., M. Mousavi Baygi, A. Alizadeh, A. N. Ziaei, and M. Bannayan. 2017. "Estimating major crop water productivity at Neyshabour basin and optimize crop area." *J. Water and Soil* 31 (1): 112–126. https://doi.org/10.22067/jsw.v31i1.58343.

Pourmohamad, Y., A. Shahnazari, A. R. Emadi, and M. Z. Ahmadi. 2011. "Effect of dredging of wetlands on variation of water allocation in Alborz dam watershed using WEAP model." *J. Watershed Manage. Res.* 2 (4): 44–56.

rShamir, E., D. M. Meko, N. E. Graham, and K. P. Georgakakos. 2007. "Hydrologic model framework for water resources planning in the Santa Cruz River, Southern Arizona 1." *J. Am. Water Resour. Assoc.* 43 (5): 1155–1170.

Ramón-Reinozo, M., D. Ballari, J. J. Cabrera, P. Crespo, and G. Carrillo-Rojas. 2019. "Altitudinal and temporal evapotranspiration dynamics via remote sensing and vegetation index-based modelling over a scarce-monitored, high-altitudinal Andean páramo ecosystem of southern Ecuador." *Environ. Earth Sci.* 78 (11): 340. https://doi.org/10.1007/s12665-019-8337-6.

R Core Team. 2013. *R: A language and environment for statistical computing*. Vienna, Austria: Citeseer.

Schmugge, T. J., W. P. Kustas, J. C. Ritchie, T. J. Jackson, and A. Rango. 2002. "Remote sensing in hydrology." *Adv. Water Resour.* 25 (8–12): 1367–1385. https://doi.org/10.1016/S0309-1708(02)00065-9.

Scott, R. 2016. *FLUXNET2015 US-Wkg Walnut Gulch Kendall Grasslands*. Washington, DC: FluxNet, USDA. http://doi.org/10.18140/FLX/1440096.

Shafian, S., and S. J. Maas. 2015. "Index of soil moisture using raw Landsat image digital count data in Texas High Plains." *Remote Sens.* 7 (3): 2352–2372. https://doi.org/10.3390/rs70302352.

Silva, A. M., R. M. da Silva, and C. A. G. Santos. 2019. "Automated surface energy balance algorithm for land (ASEBAL) based on automating endmember pixel selection for evapotranspiration calculation in MODIS orbital images." *Int. J. Appl. Earth Obs. Geoinf.* 79 (Jul): 1–11. https://doi.org/10.1016/j.jag.2019.02.012.

Singh Rawat, K., S. Kumar Singh, A. Bala, and S. Szabó. 2019. "Estimation of crop evapotranspiration through spatial distributed crop coefficient in a semi-arid environment." *Agric. W7ater Manage.* 213 (Jun): 922–933. https://doi.org/10.1016/j.agwat.2018.12.002.

Smith, R. B. 2010. *The heat budget of the earth's surface deduced from space*. New Haven, CT: Ronald B. Smith.

Trenberth, K. E., and D. J. Shea. 2005. "Relationships between precipitation and surface temperature." *Geophys. Res. Lett.* 32 (14): 1–4. https://doi.org/10.1029/2005GL022760.

USGS. 2012. "USGS global visualization viewer." Accessed December 5, 2019. http://glovis.usgs.gov/index.shtm%5Cnhttp://glovis.usgs.gov/.

Vidal, A., Y. Kerr, J. P. Lagouarde, and B. Seguin. 1987. "Remote sensing and water balance: combined use of an agro-meteorological model and thermal IR data from the NOAA-AVHRR satellite." *Agric. For. Meteorol.* 39 (2–3): 155–175. https://doi.org/10.1016/0168-1923(87)90034-7.

Yu, X., X. Guo, and Z. Wu. 2014. "Land surface temperature retrieval from Landsat 8 TIRS-comparison between radiative transfer equation-based method, split window algorithm and single channel method." *Remote Sens.* 6 (10): 9829–9852. https://doi.org/10.3390/rs6109829.

Zhang, K., J. S. Kimball, and S. W. Running. 2016. "A review of remote sensing based actual evapotranspiration estimation." *Wiley Interdiscip. Rev.: Water* 3 (6): 834–853. https://doi.org/10.1002/wat2.1168.

Zhao, L., J. Xia, C. Xu, Z. Wang, L. Sobkowiak, and C. Long. 2013. "Evapotranspiration estimation methods in hydrological models." *J. Geog. Sci.* 23 (2): 359–369. https://doi.org/10.1007/s11442-013-1015-9.

Zitouna-Chebbi, R., L. Prévot, A. Chakhar, M. Marniche-Ben Abdallah, and F. Jacob. 2018. "Observing actual evapotranspiration from flux tower eddy covariance measurements within a hilly watershed: Case study of the Kamech site, Cap Bon Peninsula, Tunisia." *Atmosphere* 9 (2): 68. https://doi.org/10.3390/atmos90200680.